Check for updates

Unraveling atomic-scale origins of interfacial properties in CsPbBr₃/M₂O₅ (M = Nb, Ta) heterojunctions: a combined first-principles and experimental approach

Menglong Gao, [ab] Yao Guo, ![ID] *[a] Shiding Zhang,[a] Yinghui Xue,[a] Jianxin Li,[a] Shuaishuai Hu,[a] Haixiang Song,[a] Kaidi Wu,[ab] Miaomiao Li,[a] Huihui Zhao,[a] Zhongyuan Zhou ![ID] *[a] and Qing Shen ![ID] *[c]

We study the interface properties of CsPbBr₃/Nb₂O₅ and CsPbBr₃/Ta₂O₅ heterojunctions for structural, electronic, and optical characteristics. First-principles calculations were performed to analyze interfacial binding energy, electronic local function (ELF), charge density difference, and electrostatic potential. Four interface configurations were constructed based on CsPbBr₃ (100) and M₂O₅ (001) terminations, revealing that the PbBr/TaO interface exhibits the highest binding energy (0.0073 eV Å^{-2}), indicating superior stability. Charge transfer calculations demonstrate electron migration from CsPbBr₃ to M₂O₅, forming an internal electric field that promotes charge separation. ELF and charge density difference maps highlight strong covalent interactions at the interfaces, particularly in the PbBr/TaO interface. Experimental characterization via XRD, SEM, TEM and XPS confirms successful heterojunction formation with preserved crystallinity. These findings provide theoretical and experimental insights into optimizing M₂O₅-based electron transport layers to enhance PSC efficiency and stability.

New concepts

This study demonstrates a rational interface engineering strategy for CsPbBr₃/M₂O₅ (M = Nb, Ta) heterostructures through combined first-principles calculations and experimental validation, addressing critical gaps in perovskite optoelectronics. While CsPbBr₃ exhibits ideal photovoltaic properties but suffers from phase instability, and M₂O₅ shows superior stability and charge transport capabilities over conventional TiO₂, the atomic-scale mechanisms governing their interfacial synergy remained unexplored. Our breakthrough lies in systematically analyzing four distinct interface configurations between M₂O₅ and CsPbBr₃'s surface terminations, revealing that interfacial charge transfer creates a built-in electric field while oxygen vacancies in M₂O₅ critically modulate interface stability. This fundamentally differs from previous empirical studies by establishing termination-dependent structure–property relationships and quantifying defect-mediated interfacial dynamics. The work provides transformative insights into CsPbBr₃/M₂O₅ interface engineering, demonstrating how atomic-level design of charge redistribution and defect control can enhance device performance. Previous research on CsPbBr₃-based heterojunctions focused on macroscopic metrics like device efficiency at the macroscale. In contrast, our work links termination-specific interfacial structures to macroscopic properties such as stability and charge transport, enabling rational design. By bridging theoretical prediction (identifying optimal hexagonal-phase M₂O₅ interfaces) with experimental synthesis/characterization, we establish a paradigm for developing stable, high-efficiency perovskite optoelectronic devices through tailored heterojunction architectures, potentially displacing conventional TiO₂.

1. Introduction

In recent years, perovskite materials have become multifunctional materials in many fields. Owing to their outstanding photoelectric conversion efficiency and tunable photoelectric properties, they have garnered considerable attention in the scientific community. Their unique photovoltaic properties endow them with the potential to be applied in next-generation technologies for advanced electronic devices, such as perovskite solar cells (PSCs) and LEDs.[1–4] The all-inorganic perovskite material CsPbBr₃ exemplifies the potential of inorganic perovskites in balancing performance and stability for next-generation optoelectronics.[5–7] In particular, template-assembled large-size CsPbBr₃ nanocomposite thin films are currently regarded as one of the most promising candidates for X-ray scintillators, while zirconia-coated CsPbBr₃ nanocrystals find applications in the field of visible light communication. Additionally, ligand-modified quantum dots are utilized in more efficient and high-color-rendering light-emitting diodes.[8–10] The PSCs have been widely studied and developed by virtue of their excellent performance and environment-friendly characteristics and the power conversion efficiency (PCE).[11,12] The structure of PSCs is generally composed of a

[a] *Henan International Joint Laboratory of Nanocomposite Sensing Materials, Anyang Institute of Technology, Anyang, 455000, China. E-mail: guoyao@ayit.edu.cn, 20200038@ayit.edu.cn*

[b] *College of Chemistry and Chemical Engineering, Henan Polytechnic University, Jiaozuo, 454003, China*

[c] *Faculty of Informatics and Engineering, The University of Electro-Communications, Tokyo, 182-8585, Japan. E-mail: shen@pc.uec.ac.jp*

substrate, transparent conductive electrode, electron transport layer (ETL), perovskite absorption layer, hole transport layer (HTL) and a metal electrode.[13–15] The ETL in PSCs is responsible for extracting electrons from the perovskite absorption layer and preventing holes from migrating to the transparent conductive electrode, thereby minimizing charge recombination at the interface. However, although the current energy conversion efficiency of PSCs has been greatly recognized, their performance is still deteriorated by charge carrier recombination.[16,17] Therefore, among the many factors that affect the PCE of PSCs, preventing and reducing carrier recombination at the interfaces is of particular importance. So, the ETL and HTL play a role in promoting the extraction of electrons and holes and blocking the transport of opposite charges, effectively improving the performance and efficiency of PSCs.[18–20] The microscopic architecture of the ETL facilitates perovskite crystallization and film formation while shortening the migration pathway of photogenerated electrons. Additionally, a suitable ETL must exhibit energy band alignment compatible with the perovskite material.[21,22] Thus, strategic ETL material selection serves as a cornerstone for achieving both high efficiency and operational stability in perovskite optoelectronic devices. Many studies are devoted to the development of high-performance PSCs by finding new materials and interface modification methods. Metal oxides are predominantly utilized as the ETL in perovskite optoelectronics due to their tunable band alignment and robust charge extraction capabilities. The most commonly used metal oxides for an ETL are TiO_2, ZnO, SnO_2 and ZrO_2.[23–26] At the same time, many electron transport materials are prone to degradation and aging under long-term environmental conditions such as light and thermal radiation, leading to a decline in electron transport performance, affecting the stability and service life of PSCs.[27–29] Further research is needed to improve the device performance by means of interface modification and the search for more suitable oxides.

Niobium and tantalum pentoxides (Nb_2O_5 and Ta_2O_5) possess excellent chemical stability and optical properties, suitable for optical materials, electronic devices, and ceramics.[29–31] As promising ETL alternatives to TiO_2 in PSCs, Nb_2O_5 exhibits a suitable band gap, high carrier mobility, better chemical stability than TiO_2, and room-temperature processability enabling flexible large-area devices;[32,33] Ta_2O_5 exhibits the aforementioned advantageous properties and effectively suppresses charge recombination and enhances the PCE.[34–36] Their hexagonal crystal structure is widely used in optoelectronics.[37–39] Therefore, both are promising as ETL materials for PSCs to replace the current TiO_2 materials.[40,41] However, compared with other metal oxides, M_2O_5 research remains incomplete, with insufficient understanding of heterojunction interfacial characteristics (microstructure evolution, charge transfer dynamics, and bonding mechanisms).[42] Computational simulations can provide atomic-scale insights,[43] facilitating rational design of high-performance optoelectronic devices via interface engineering.

In this study, we constructed interface models for $CsPbBr_3$/Nb_2O_5 and $CsPbBr_3$/Ta_2O_5. To understand the interfacial properties, we designed four types of interfaces and calculated their characteristics.[44] First-principles calculations were performed to analyze and investigate the stability, electronic, and optical properties of the $CsPbBr_3$/Nb_2O_5 and $CsPbBr_3$/Ta_2O_5 interfaces. $CsPbBr_3$/M_2O_5 heterojunction samples were synthesized, and their structure and morphology were characterized. Meanwhile, X-ray photoelectron spectroscopy (XPS) was used to analyze the charge transfer. Furthermore, the photoelectrochemical properties of the heterojunction devices were tested, validating the theoretical calculations. This study is anticipated to provide critical insights into the fundamental characteristics of $CsPbBr_3$/M_2O_5 systems, while optimizing their photoelectric properties, thereby advancing the rational design and practical implementation of perovskite optoelectronic devices.

2. Computational and experimental details

2.1. Computational details

The theoretical part of the study was conducted using the Vienna *ab initio* simulation package, based on density-functional theory (DFT).[45] The GGA-PBE exchange–correlation function was employed to describe the interactions.[46] The first Brillouin zone integration was sampled using the Monkhorst–Pack *k*-point mesh. The plane-wave cutoff energy was set at 450 eV and the electronic iteration convergence was 1×10^{-6} eV, using Gaussian smearing with a width of 0.05 eV. The crystal structure of $CsPbBr_3$ with a space group of $Pm3m$ was chosen for constructing. Additionally, Nb_2O_5 and Ta_2O_5 are in the hexagonal phase with a space group of $P6/mmm$. The crystallographic configurations of $CsPbBr_3$ and M_2O_5 systems are described in the SI (Fig. S1 and Table S1), providing foundational structural data for subsequent analyses. Based on previous experimental studies, it has been reported that the M_2O_5 (001) and $CsPbBr_3$ (100) planes grow crystal interfaces in this direction while forming the interface between the two materials.[47,48] Therefore, the M_2O_5 (001) surface and the $CsPbBr_3$ (100) surface were selected to form a heterogeneous structure through perovskite lattice surface coupling. In this study, the interface model is established by superimposing $CsPbBr_3$ and M_2O_5 surface models. $CsPbBr_3$ can adopt two distinct surface terminations: the CsBr-terminated surface and the PbBr-terminated surfaces, which arise from different cleavage planes in the crystal structure. Consequently, four distinct interfacial configurations were systematically constructed through combinations of the two material systems: CsBr–NbO, PbBr–NbO, CsBr–TaO, and PbBr–TaO. The interface model adheres to the stoichiometric ratio, and the descriptions of the interfaces are listed in Fig. S2. The interface model is constructed from oxide and perovskite layers, resulting in average absolute strains of approximately 1.29% and 1.34%, respectively. The vacuum layer of 15 Å was applied in the *z*-direction to eliminate fictitious interactions between periodic images. During geometric optimization, the bottom three M_2O_5 layers were frozen to their bulk geometry, while the remaining layers were fully relaxed. The VESTA software was utilized to visualize all the structural and volumetric data.[49]

2.2. Synthesis of M$_2$O$_5$

The previous synthesis methods, such as hydrothermal and sol–gel techniques, were expensive and difficult to implement.[37,50,51] In this study, hexagonal tantalum oxide was successfully prepared through the thermal decomposition and oxidation of tantalum chloride.[52] For the synthesis of Nb$_2$O$_5$, XRD measurements were conducted on samples prepared under various conditions during preliminary experiments. Analysis results in Fig. S7 show that the product calcined at 580 °C for 3 hours exhibits a diffraction pattern that matches well with the standard reference card (JCPDS No. 28-317). Therefore, we determined the optimal temperature for preparing hexagonal niobium oxide and subsequently synthesized a niobium oxide sample. Niobium pentachloride (NbCl$_5$) (99.9%, Macklin) and tantalum pentachloride (TaCl$_5$) (99.9%, Macklin) were used as precursors. Specifically, TaCl$_5$ was calcined for 2 hours at 500 °C, while NbCl$_5$ required 3 hours at 580 °C. The precursors were calcined in crucibles at heating rates of 5 °C min^{-1}. After calcination, the products were cooled to room temperature to obtain Ta$_2$O$_5$ and Nb$_2$O$_5$. During this process, chlorine in the precursors was removed through high-temperature oxidation.

2.3. Synthesis of CsPbBr$_3$/M$_2$O$_5$

We obtained the compound using the *in situ* one-pot method. In a nitrogen atmosphere, the precursor was prepared by heating 30 mL of oleic acid and 0.843 g of cesium carbonate (AR, Aladdin) to 120 °C for 1 h, until the powder is completely dissolved and the precursor is yellowish. 0.00075 mol M$_2$O$_5$ and 0.0015 mol lead bromide powder (AR, Aladdin) were weighed and added to a 50 mL three-neck flask with 1.8 mL of oleic acid (≥99 wt%, Macklin), 1.8 mL of oleamine (90 wt%, Macklin) and 20 mL of octadecene solvent (≥95 wt%, Macklin). The mixture was stirred at 800 rpm, forming a milky white solution. When heated to 180 °C for 1 h, 3 mL of the precursor was quickly injected, causing the solution to immediately turn yellow-green. After 15 s of reaction, the three-neck flask was removed and placed in an ice water bath to cool the mixture to room temperature. The product was washed and centrifuged three to five times with *n*-hexane and anhydrous ethanol, followed by vacuum drying at 80 °C for 12 hours. The compound of perovskite and oxide was successfully obtained. The synthesis process is described in Fig. 1.

3. Results and discussion

3.1. Interfacial energy

The interfacial binding energy serves as a quantitative metric for evaluating the adhesive interactions at material junctions, where its magnitude correlates with both the robustness of atomic-scale bonding and the stability of the interfacial region. This thermodynamic parameter fundamentally represents the work needed to cleave an intact interface into two isolated surfaces. The following formula can be used to describe the bonding energy:

$$E_{\text{binding}} = [E_{\text{perovskite}} + E_{\text{M}_2\text{O}_5} - E_{\text{total}}]/A \qquad (1)$$

where $E_{\text{perovskite}}$ and $E_{\text{M}_2\text{O}_5}$ represent the total energy of the perovskite and M$_2$O$_5$ surfaces after full relaxation, respectively. E_{total} denotes the total energy of the CsPbBr$_3$/M$_2$O$_5$ interface and A is the surface area of the interface. The calculated E_{binding} values of CsPbBr$_3$/M$_2$O$_5$ interfaces are listed in Table 1. In our results, there are four interfacial configurations with the positive binding energy that indicates the formation of a stable heterojunction structure. Therefore, it can be concluded that the stable interface structures are composed of CsPbBr$_3$/M$_2$O$_5$.[53]
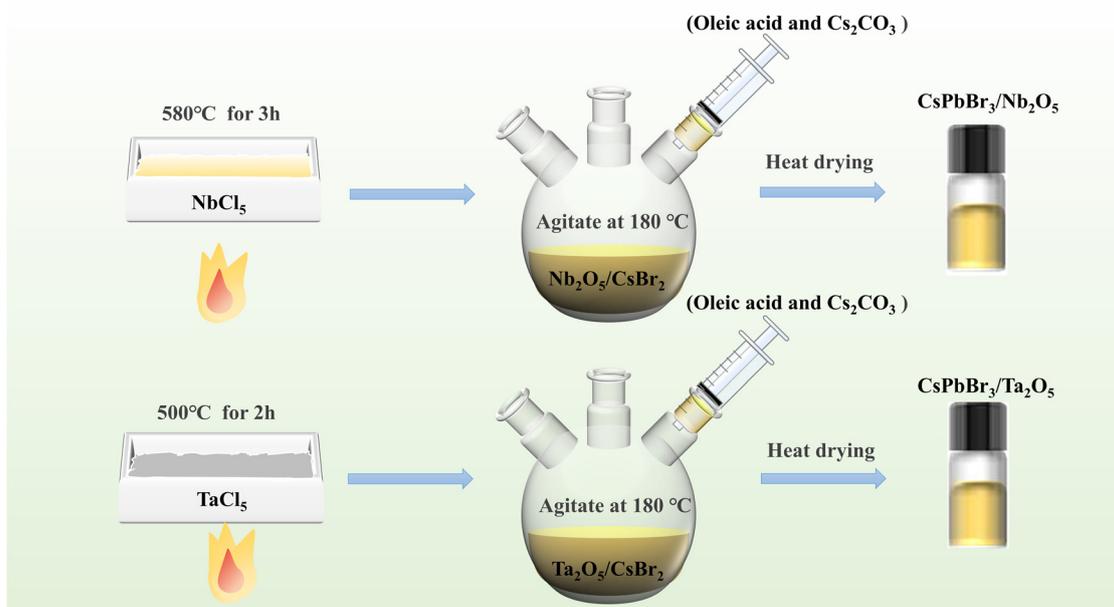

Fig. 1 The schematic diagram for the synthesis of CsPbBr$_3$/M$_2$O$_5$.

Table 1 Calculated interfacial energies (eV Å^{-2}), charge transfer (e), potential drops (eV) and work functions (eV) of the relaxed CsPbBr$_3$/M$_2$O$_5$ interfaces

	Interfacial energy	Charge transfer	Potential drop	Work function
CsBr/NbO	0.0022	0.173	5.29	4.36
PbBr/NbO	0.0021	0.108	5.09	4.81
CsBr/TaO	0.0053	0.166	2.70	3.68
PbBr/TaO	0.0073	0.104	2.54	4.09

The interfacial stability follows the sequence of PbBr/TaO, followed by CsBr/TaO, CsBr/NbO, and finally PbBr/NbO, as quantified by binding energy calculations and structural integrity assessments. At the same time, the binding energy of CsPbBr$_3$/Ta$_2$O$_5$ is obviously greater than that of CsPbBr$_3$/Nb$_2$O$_5$, indicating that the stability and difficulty of the formation of a heterojunction between the perovskite and the two oxides are different, and the combination with CsPbBr$_3$/Ta$_2$O$_5$ is more stable and easier to form. Furthermore, it is found that the difference in $E_{binding}$ between the two interfaces (CsBr/NbO and PbBr/NbO) formed in the CsPbBr$_3$/Nb$_2$O$_5$ system and the two interfaces (CsBr/TaO and PbBr/TaO) in the CsPbBr$_3$/Ta$_2$O$_5$ system are relatively small. This indicates that the stabilities of the two end-face configurations in CsPbBr$_3$/Nb$_2$O$_5$ are quite comparable, while significant differences exist between the two interfaces in CsPbBr$_3$/Ta$_2$O$_5$. Overall, the PbBr/TaO interfacial model with a binding energy of 0.0073 eV Å^{-2} configuration demonstrates exceptional interfacial stability and is the most stable heterostructure among these four models as it exhibited the highest binding energy. The most stable PbBr/TaO interface would reduce the possibility of interfacial atom diffusion or detachment and further inhibits the potential degradation of PSCs. Accordingly, the device lifetime can also be improved through the regulation of interface engineering.

3.2. Electronic properties

The ELF was calculated to understand the bonding mechanism of the CsPbBr$_3$/M$_2$O$_5$ interfaces.[54] The contour maps of the ELF of the four CsPbBr$_3$/M$_2$O$_5$ interface models are plotted and compared in Fig. S3. The PbBr/Ta$_2$O$_5$ heterojunction exhibits the optimal interfacial stability due to the strong Pb–O bonding interaction and lattice strain adaptation. ELF analysis reveals a high degree of electron localization around Br and O atoms, whereas Cs shows stronger electron delocalization, indicating its weaker participation in covalent bonding. Compared with Nb$_2$O$_5$, the Pb–O bonds at the Ta$_2$O$_5$ interface are shorter with a higher charge density overlap. Meanwhile, the PbBr/Ta$_2$O$_5$ interface exhibits the most pronounced lattice distortion, which is directly correlated with its highest interfacial binding energy. Based on the ELF results, we can prioritize the selection of oxide materials that can form strong covalent interactions with perovskite components as the interface modification layer, thereby fundamentally improving the long-term operational stability of PSCs.

To further explore the electronic coupling properties and charge redistribution, we calculated the three-dimensional and plane-averaged charge density difference ($\Delta\rho$). These calculations provide an intuitive visualization of the electronic state distribution, as depicted in Fig. 2. It was observed that the yellow regions at the interface, representing electron accumulation, were primarily located on the oxide surface, while the green regions, indicating electron depletion, were concentrated below the Cs and Br atoms. These observations suggest that at the interface, the perovskite acts as an electron donor and M$_2$O$_5$ serves as an electron acceptor. The pronounced charge redistribution phenomenon was identified at the CsBr/M$_2$O$_5$ interface, and CsBr/M$_2$O$_5$ shows more obvious charge reconfiguration and redistribution compared to PbBr/M$_2$O$_5$. In addition, above mentioned charge transfer and redistribution also show consistent results in the plane-averaged charge density difference ($\Delta\rho$) of the CsPbBr$_3$/M$_2$O$_5$ heterojunction, where positive values of $\Delta\rho$ indicate electron enhancement, and negative values indicate electron loss. And it also again corresponds to the charge transfer values presented in Table 1. We calculated the charge transfer values based on the Bader charge analysis for four models. Positive values reveal electron transfer from CsPbBr$_3$ to M$_2$O$_5$. Interestingly, among the four interfaces, CsBr/NbO and CsBr/TaO have better electron transport performance, but their structural stability is not as good as PbBr/TaO. The interfacial charge transfer depends on the
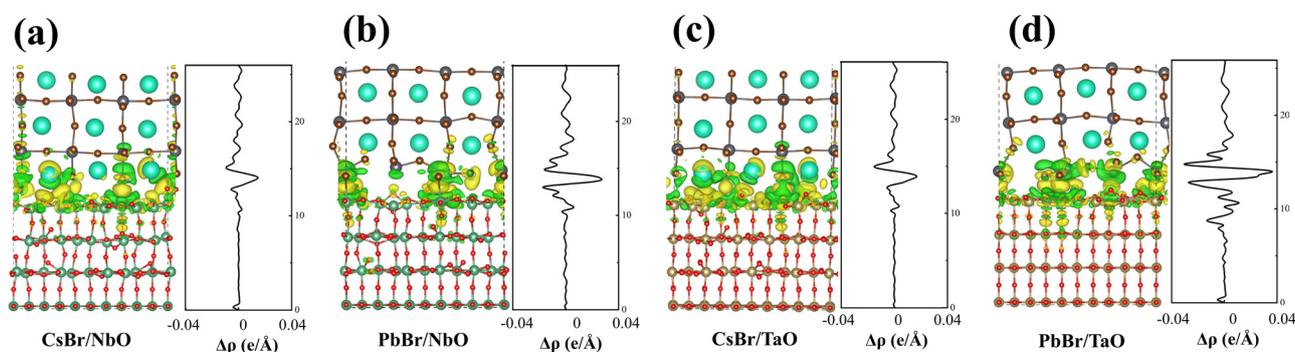

Fig. 2 Schematic diagram illustrating the transfer of charges at the interface, isosurfaces and plane-averaged charge density difference ($\Delta\rho$) for the CsPbBr$_3$/M$_2$O$_5$ models of (a) CsBr/Nb$_2$O$_5$, (b) PbBr/Nb$_2$O$_5$, (c) CsBr/Ta$_2$O$_5$, and (d) PbBr/Ta$_2$O$_5$ where the isosurface levels are at 0.001 e Å^{-3}.

surface termination of the perovskite rather than that of M_2O_5. Such changes in terminal atoms can alter local charge distribution and interfacial interactions, thereby leading to observable disparities in charge behavior.

The perovskite layer and M_2O_5 substrate, with distinct functional properties, induce charge redistribution at their interface, forming a strong dipole moment at the heterojunction, while the inherent potential gradient generates a built-in electric field driving directional charge separation. Planaraveraged electrostatic potential along the z-axis for all four interfaces (Fig. S4) reveals that the perovskite layer has higher potential than the oxide layer, and $CsBr/M_2O_5$ interfaces show a larger potential offset than $PbBr/M_2O_5$, synergistically suppressing electron–hole recombination by enhancing carrier separation. Quantitative analysis of potential drops and work functions (Table 1) indicates that $PbBr/M_2O_5$ has higher work function than $CsBr/M_2O_5$, which shows larger potential drops. Notably, the PbBr/TaO interface in $CsPbBr_3/Ta_2O_5$, with the lowest work function and near-maximal binding energy, ensures efficient charge extraction and robust stability, being optimal for stable heterojunction design.

To further investigate the interfacial properties of the $CsPbBr_3/M_2O_5$ heterostructure, the total density of states (DOS) of four interfaces was calculated. Additionally, we calculated the partial DOS for the atoms in the three interfacial layers of the perovskite and oxide separately. These calculations allow us to clearly understand how each atomic layer at the interface contributes to the distribution of electronic states and the formation of interfacial states within these heterojunctions, as shown in Fig. 3 and Fig. S5. The results demonstrate that the oxide layer at the interface exhibits more prominent valence band contributions, which can be attributed to the contributions from O atoms in the oxide. Meanwhile, the oxide also

shows significant conduction band contributions due to the role of Nb and Ta atoms, with additional contributions from Pb, and the contributions of Cs to both the valence band and conduction band are negligible. This phenomenon is likely caused by electron transfer from the perovskite to oxide, leading to the Fermi level of oxide dominating the band structure near the interface. Additionally, strong hybridization is detected between O and Br atoms, revealing a robust covalent bonding interaction at the interface. This finding aligns with the previous ELF analysis results. Furthermore, it was observed that CsPb atomic layers in all interfaces of the $CsPbBr_3/M_2O_5$ system exhibit greater valence band contributions, which is attributed to the contribution of Pb atoms. A notable trend was identified across all interfaces: with increasing distance from the interface, the oxide layers show incremental peak contributions to both the valence and conduction bands near the Fermi level, particularly evident in the $PbBr/Ta_2O_5$ interface. This suggests the emergence of new electronic states near the Fermi level, likely originating from interface or defect states, which detrimentally affect electron transport. These observations align with the Bader charge analysis results. DOS calculations reveal strong covalent bonding between Br and O atoms at the interface, peak contributions of different atomic layers to the conduction and valence bands, and the emergence of new defect states at the interface. These findings provide a basis for optimizing the performance of perovskite optoelectronic devices by guiding the selection of optimal interfacial configurations.

3.3. Optical properties

Optical properties play a critical role in elucidating the fundamental characteristics of materials and probing their optoelectronic behavior, which is essential for optoelectronic devices. We systematically studied the optical properties of four
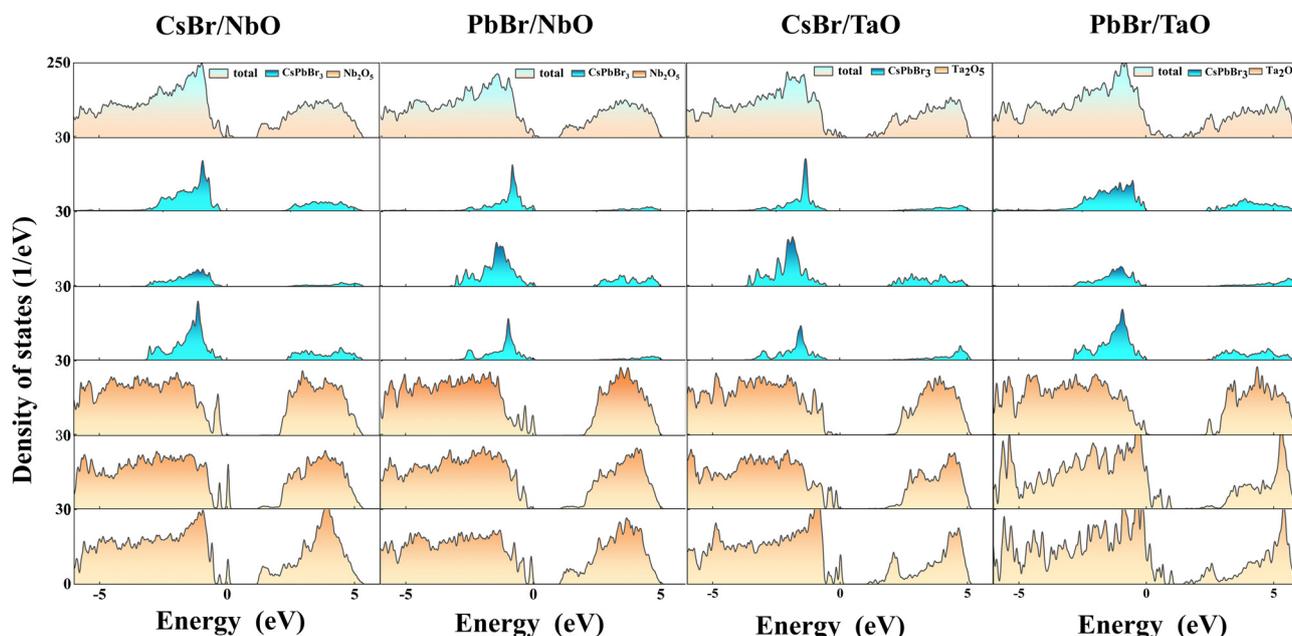

Fig. 3 The calculated DOS plots for the (a) $CsBr/Nb_2O_5$, (b) $PbBr/Nb_2O_5$, (c) $CsBr/Ta_2O_5$, and (d) $PbBr/Ta_2O_5$ interfacial models.

interface models by calculating the dielectric functions of the $CsPbBr_3$/M_2O_5 heterostructure within the energy range of 0–15 eV, providing insights into understanding and comparing the polarization response, interface stability, and light absorption characteristics of the $CsPbBr_3$/M_2O_5 interface.[55,56] As shown in Fig. 4, the real (ε_1) and imaginary (ε_2) components of the dielectric function for the four interface models are displayed in the upper and lower panels, respectively. At zero energy, the static dielectric function (electronic contribution) exhibits the highest value of ε_1 = 5.78 for the $CsBr$/Nb_2O_5 interface and the lowest value of ε_1 = 3.82 for $CsBr$/Ta_2O_5. The ε_1 spectra of the four interface models exhibit a consistent trend, all reaching their maxima around 2.5 eV ($\varepsilon_1 \approx$ 5.8). Notably, the $CsPbBr_3$/Ta_2O_5 interface demonstrates a higher ε_1 peak frequency compared to $CsPbBr_3$/Nb_2O_5, followed by a gradual decrease to lower values for $CsBr$/TaO. This indicates that the polarization process at the $CsPbBr_3$/Ta_2O_5 interface responds more rapidly to electric field variations, suggesting faster polarization dynamics. Appropriate polarization effects may contribute to stabilizing the crystal structure of the material. The imaginary part of the dielectric function (ε_2) correlates with the optical absorption coefficient. Small peaks observed at approximately 0.25 eV in the $\varepsilon_2(\omega)$ spectra of $CsBr$/NbO, $PbBr$/NbO, and $PbBr$/TaO interfaces can be attributed to inter band optical transitions induced by photons with sufficient energy to excite electronic transitions. Enhanced absorption peaks emerge sequentially in the 2.5–6 eV energy range across all four interface models. In particular, the $PbBr$/M_2O_5 interface exhibits two distinct peaks, with the $PbBr$/Ta_2O_5 interface showing more pronounced peak intensities than $PbBr$/Nb_2O_5. These spectral features originate from interband transitions between O p-states in the valence band and M (Nb or Ta) d-states in the conduction band. The $PbBr$/Ta_2O_5 interface exhibits a significantly enhanced absorption peak at ~6 eV compared to $PbBr$/Nb_2O_5, while the $CsBr$/Ta_2O_5 interface shows a stronger 3 eV peak relative to $CsBr$/Nb_2O_5. These results indicate that the $CsPbBr_3$/Ta_2O_5 heterostructure exhibits superior light-harvesting capability at their respective characteristic photon energies. By regulating the interface, the light absorption capacity is enhanced, which further improves the light-trapping efficiency, thereby achieving a significant enhancement in device performance.

3.4. Oxygen vacancy

Defect states and energy level alignments govern charge carrier dynamics in optoelectronic devices, which is pivotal to unlocking the full potential of perovskite semiconductors. Given the intrinsic propensity for oxygen vacancy formation in hexagonal oxides,[57–60] we established computational models with oxygen vacancies at the $CsPbBr_3$/M_2O_5 interface to assess their impact on interfacial stability. In particular, oxygen atoms were selectively removed from the M_2O_5 layer in relaxed heterojunctions. The total energies of five different oxygen vacancy configurations across the four interface models were determined through calculations, as summarized in Fig. 5. Relaxation energy analysis revealed that negative total energy values correlate with enhanced structural stability, where more negative energies indicate stronger interatomic bonding. Notably, the TaO/$PbBr$ interface exhibited the highest total energy (i.e., most negative value) among the investigated systems. This indicates that the TaO/$PbBr$ interface is the most stable among the four interface models. Additionally, for the remaining three interfaces, oxygen vacancies in 1, 3 and 5 layers exhibit greater stability than those in 2 and 4 layers, which is attributed to the distinct positions of oxygen vacancies: pure O atomic layers versus layers containing Ta–O atom bonds. Therefore, the relationship between oxygen vacancy positions and interfacial stability was determined through systematic defect engineering of $CsPbBr_3$/M_2O_5 heterostructures.

3.5. Crystal structure and morphology

To validate our computational results, we synthesized $CsPbBr_3$, Nb_2O_5, Ta_2O_5, and $CsPbBr_3$/M_2O_5 heterojunction samples, which were characterized by XRD, SEM, and TEM as shown in Fig. 6. The distinct diffraction peaks detected in the M_2O_5 and $CsPbBr_3$ samples suggested a high degree of crystallinity within these samples. The XRD patterns recorded for the Nb_2O_5, Ta_2O_5, $CsPbBr_3$ and $CsPbBr_3$/M_2O_5 samples are presented in Fig. 6a. The diffraction peaks at 2θ = 15.3°, 21.5° and 30.5° correspond to the (100), (110) and (200) crystal faces of $CsPbBr_3$ (PDF#18-0364), respectively. The peaks found at 2θ = 22.6° and 28.5° correspond to the (001) and (100) crystal faces of Nb_2O_5 (JCPDS#28-0317) and 2θ = 22.9° and 28.4° correspond to the (001) and (100) crystal faces of Ta_2O_5 (JCPDS # 9-1299). The XRD spectra of the $CsPbBr_3$/M_2O_5 heterostructure exhibit distinct diffraction peaks corresponding to both cubic $CsPbBr_3$ and hexagonal M_2O_5 phases, confirming the successful formation of the heterojunction. It is worth noting that the diffraction peak intensity of Nb_2O_5 in the $CsPbBr_3$/Nb_2O_5 composite structure is significantly lower than that of Ta_2O_5 in $CsPbBr_3$/Ta_2O_5. This phenomenon is mainly attributed to the following factors: the crystallinity of Nb_2O_5 itself is not as good as that of Ta_2O_5, which can be observed in the XRD pattern where the peaks of Nb_2O_5 are weaker than those of Ta_2O_5. The average size of Nb_2O_5 crystalline particles is significantly smaller than that of Ta_2O_5 particles, which is
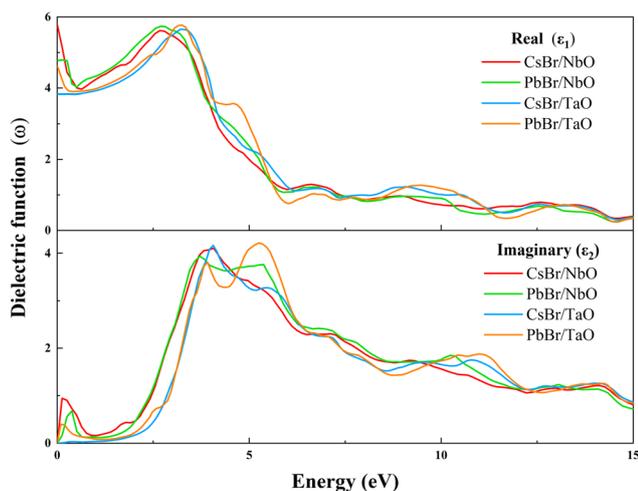

Fig. 4 Real and imaginary parts of the dielectric functions for the relaxed $CsPbBr_3$/M_2O_5 heterojunctions.
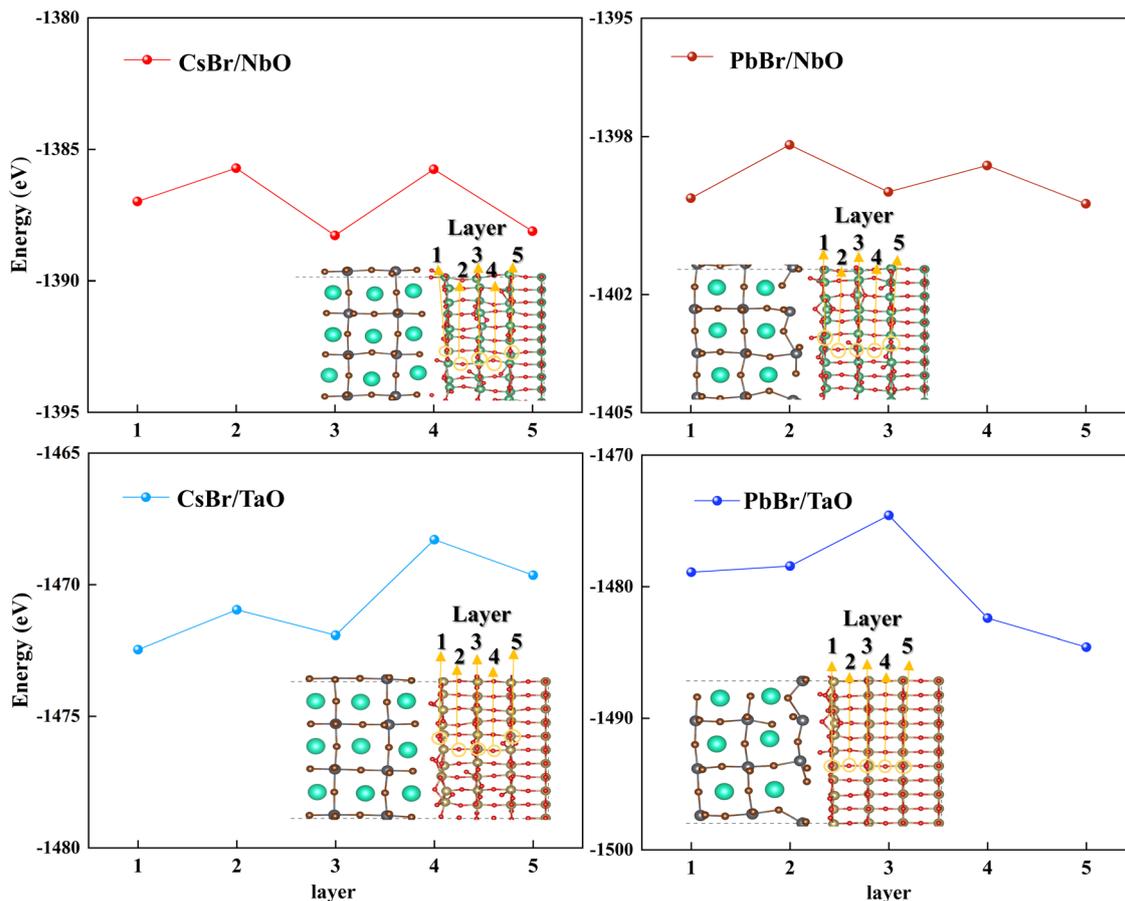
Fig. 5 Schematic diagram illustrating the side view diagram of the oxygen vacancy structure and the oxygen vacancy model energy.

consistent with the SEM image. Meanwhile, during the preparation of the composite sample, the formation of $CsPbBr_3$ in the composite process may cause a reduction in grain size, resulting in decreased peak intensity.
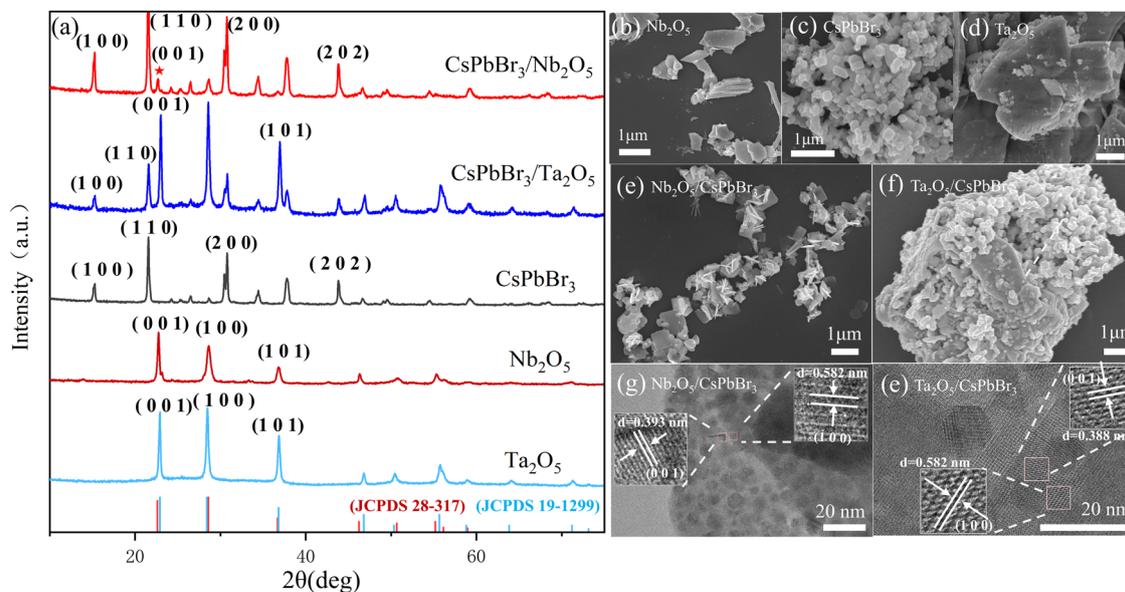

Fig. 6 (a) The XRD patterns for $CsPbBr_3$, Nb_2O_5, Ta_2O_5, and the $CsPbBr_3/M_2O_5$. The SEM images for (b) Nb_2O_5, (c) $CsPbBr_3$ (d) Ta_2O_5, (e) $CsPbBr_3/Nb_2O_5$, and (f) $CsPbBr_3/Ta_2O_5$. The TEM images (g) for $CsPbBr_3/Nb_2O_5$ and (h) $CsPbBr_3/Ta_2O_5$.

Furthermore, the micromorphology of the M_2O_5, $CsPbBr_3$ and the $CsPbBr_3/M_2O_5$ heterojunction materials was further investigated using SEM and TEM. The images obtained from these characterization studies are presented in Fig. 6b–h. The Nb_2O_5 sample exhibits a sharp particle nanosheet structure with no obvious defects on the surface, while the Ta_2O_5 sample shows large crystalline particles, as demonstrated by the SEM images in Fig. 6b and d. The $CsPbBr_3$ sample, which displays a square structure, is shown in Fig. 6c. In Fig. 6e and f, it can be observed that $CsPbBr_3$ nanocrystals are uniformly dispersed on the surface of oxide particles. As shown in Fig. 6g and h, TEM analysis revealed that after the formation of $CsPbBr_3$ nanocrystals, distinct lattice fringes corresponding to the (100) plane of $CsPbBr_3$ with an interplanar spacing of 0.58 nm were observed in the planar direction. Additionally, adjacent lattice fringes corresponding to the (001) planes with spacings of 0.39 nm and 0.38 nm, respectively, were also identified surrounding the Nb_2O_5 and Ta_2O_5 nanocrystals. Additionally, the elemental mapping of $CsPbBr_3/Ta_2O_5$ is presented in Fig. S8. The homogeneous distribution of Cs, Pb, Br, and Ta elements validates the formation of a well-mixed $CsPbBr_3/Ta_2O_5$ composite. These experimental results confirm that the successful synthesis of $CsPbBr_3/M_2O_5$ heterojunctions is consistent with the computational simulations.

3.6. X-ray photoelectron spectroscopy analysis

To further validate the successful synthesis of heterojunctions, characterize interfacial charge transfer behavior, and corroborate our computational results, XPS was performed on pristine $CsPbBr_3$, M_2O_5, and their composite samples. As illustrated in Fig. 7 and Fig. S6, distinct elemental characteristic peaks were observed in different samples, confirming the formation of $M_2O_5/CsPbBr_3$ heterojunctions. In the $Nb_2O_5/CsPbBr_3$ heterojunction, the Br $3d_{3/2}$ and $3d_{5/2}$ peaks exhibited binding energies of 69.25 eV and 68.18 eV with negative shifts of 0.15 eV and 0.19 eV, respectively. The corresponding negative shifts of
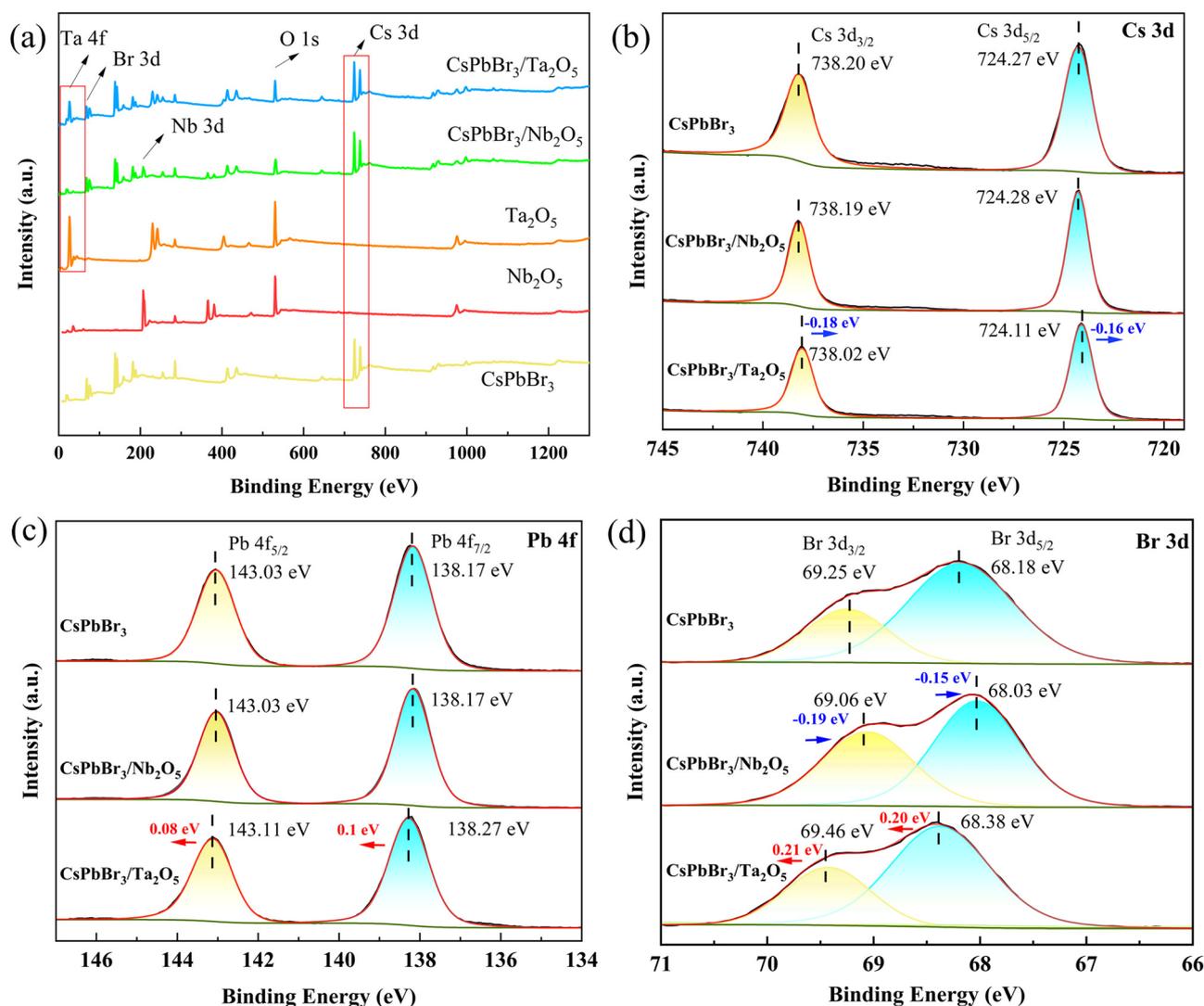

Fig. 7 (a) Survey of all the samples, both the peak position and peak shape indicate the elemental composition of the samples. (b)–(d) Cs 3d, Pb 4f, and Br 3d are displayed, respectively.
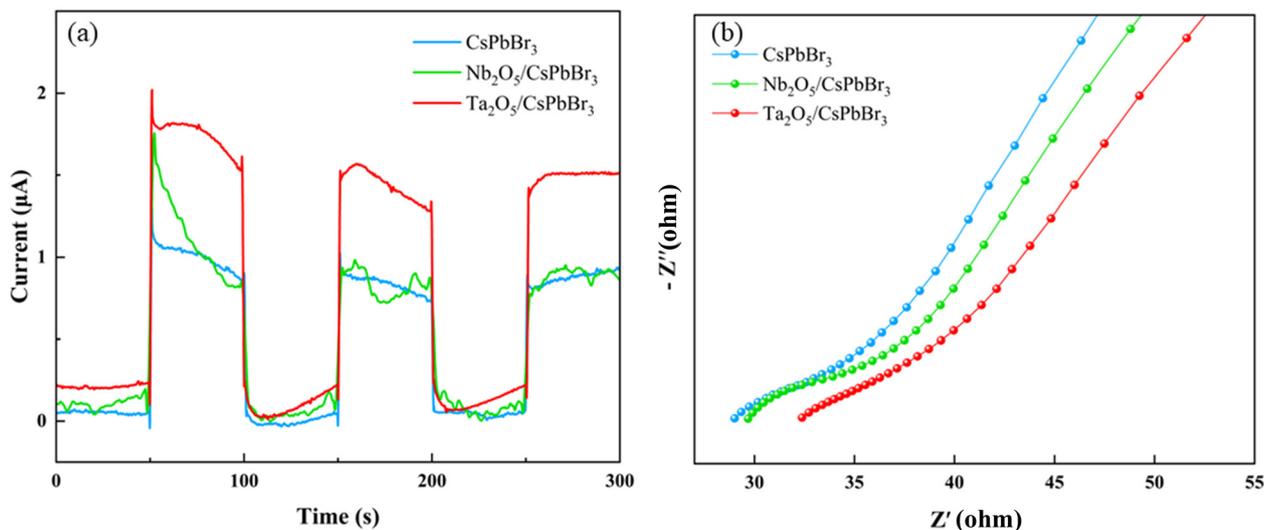
Fig. 8 (a) Transient photocurrent response density *versus* time (*i*–*t* curve) and (b) EIS spectra of $CsPbBr_3$ and $CsPbBr_3/M_2O_5$ composites.

0.18 eV and 0.20 eV were detected for Nb $3d_{7/2}$ (209.88 eV) and $3d_{5/2}$ (207.12 eV) peaks, indicating electron accumulation in Nb. Meanwhile, the O 1s peak at 530.10 eV showed a positive shift of 0.83 eV, presumably attributed to hole aggregation induced by oxygen vacancies. For the $Ta_2O_5/CsPbBr_3$ heterojunction, positive binding energy shifts were observed for Pb $4f_{5/2}$ (143.03 eV) and $4f_{7/2}$ (138.17 eV) peaks, along with Br 3d transitions, suggesting de-electronation of perovskite components. In contrast, the lattice oxygen in Ta_2O_5 displayed increased electron density (negative binding energy shift), accompanied by partial reduction of Ta^{5+} to metallic Ta as evidenced by characteristic peaks at 22.03 eV and 19.38 eV (Ta $4f_{7/2}$). These XPS results collectively demonstrate a net electron transfer from $CsPbBr_3$ to M_2O_5 across the heterojunction interface, presumably driven by the higher Fermi level of $CsPbBr_3$. This charge redistribution facilitates the formation of a built-in electric field, promoting photogenerated carrier separation in good agreement with our theoretical calculations. However, the presence of metallic Ta and adsorbed oxygen species may introduce interfacial defects, highlighting the necessity for optimized interface engineering to minimize recombination losses.

3.7. Photoelectrochemical properties

Transient photocurrent measurements and EIS were conducted to verify that the heterojunction enhances the transfer and separation efficiency of photogenerated carriers, as shown in Fig. 8. Among the tested samples, the initial current of $M_2O_5/CsPbBr_3$ is higher than that of $CsPbBr_3$ alone. It is noteworthy that the performance of $Ta_2O_5/CsPbBr_3$ remains relatively stable in subsequent cycles, while $Nb_2O_5/CsPbBr_3$ exhibits a large initial current but significant decay and fluctuation in the following cycles. This is consistent with our previous calculation results of charge transfer; meanwhile, the unstable interface leads to performance fluctuations of the material. In EIS measurements, the arc radius of $M_2O_5/CsPbBr_3$ is smaller than that of $CsPbBr_3$, indicating that the heterojunction constructed

by oxide and perovskite has lower resistance, which is more conducive to promoting charge transfer.

4. Conclusions

This study on $CsPbBr_3/M_2O_5$ (M = Nb, Ta) heterojunctions unveils critical interfacial mechanisms governing stability, electronic/optical properties, and defect tolerance, offering design guidelines for high-performance perovskite optoelectronics. The PbBr/TaO interface exhibits superior stability (binding energy: 0.0073 eV Å^{-2}) due to synergistic Pb–O covalent bonding (ELF > 0.75) and Br–Ta orbital hybridization, mitigating lattice strain. In contrast, CsBr/M_2O_5 interfaces, despite larger charge transfer values, suffer from reduced bond energies due to excessive interfacial charge redistribution, highlighting a stability-efficiency tradeoff. PDOS analysis reveals oxide-dominated conduction bands and perovskite-driven valence bands near the Fermi level, with PbBr/TaO interface states enhancing charge separation. The interface's built-in electric field and low work function promote electron extraction and suppress recombination. Dielectric function analysis shows that $CsPbBr_3/Ta_2O_5$ exhibits faster polarization response (higher ε_1 peak frequency) and stronger light absorption (more pronounced ε_2 peaks). Oxygen vacancy engineering improves stability *via* defect passivation. XRD and TEM validate phase-pure heterojunctions with lattice matching and uniform dispersion. The PbBr/TaO interface is identified as optimal for balancing mobility and stability, underscoring oxygen coordination as a key design parameter. The XPS analysis reveals that charge transfer occurs from the perovskite to the oxide at the interface of $CsPbBr_3/M_2O_5$ heterojunctions, accompanied by a net electron transfer from $CsPbBr_3$ to M_2O_5. Finally, the photoelectrochemical measurements performed on $CsPbBr_3$ and heterojunction samples demonstrate that $Ta_2O_5/CsPbBr_3$ outperforms $Nb_2O_5/CsPbBr_3$, which is consistent with our previous calculation results. Through innovative approaches, this study investigates the interfacial properties of $CsPbBr_3/M_2O_5$ heterojunctions to advance the research,

development, and exploration of more efficient and stable perovskite optoelectronic devices.

Author contributions

Conflicts of interest

The authors declare no known competing financial interests or personal relationships that could have influenced the work reported in this paper.

Data availability

All relevant data generated during this study, including DFT calculation parameters, experimental raw data, and analysis scripts, are available from the corresponding author upon reasonable request.

Supplementary information available: Crystal structures; electrostatic potential distribution profiles; planar-averaged electrostatic potential curves; partial PDOS plots; additional XPS spectra; supplementary XRD patterns; elemental mapping data; lattice parameters. See DOI: https://doi.org/10.1039/d5mh01004g

Acknowledgements

References

1 H. M. Ghaithan, Z. A. Alahmed, S. M. H. Qaid, M. Hezam and A. S. Aldwayyan, *ACS Omega*, 2020, **5**, 7468–7480.

2 Y. Chen, M. Zhang, F. Li and Z. Yang, *Coatings*, 2023, **13**, 644.

3 A. Fakharuddin, M. K. Gangishetty, M. Abdi-Jalebi, S.-H. Chin, A. R. B. Mohd Yusoff, D. N. Congreve, W. Tress, F. Deschler, M. Vasilopoulou and H. J. Bolink, *Nat. Electron.*, 2022, **5**, 203–216.

4 J. Duan, H. Xu, W. E. I. Sha, Y. Zhao, Y. Wang, X. Yang and Q. Tang, *J. Mater. Chem. A*, 2019, **7**, 21036–21068.

5 L. Protesescu, S. Yakunin, M. I. Bodnarchuk, F. Krieg, R. Caputo, C. H. Hendon, R. X. Yang, A. Walsh and M. V. Kovalenko, *Nano Lett.*, 2015, **15**, 3692–3696.

6 J. Liang, J. Liu and Z. Jin, *Sol. RRL*, 2017, **1**, 1700086.

7 S. Ullah, F. Khan and A. AlZahrani, *Coord. Chem. Rev.*, 2024, **516**, 215957.

8 B. Wang, J. Peng, X. Yang, W. Cai, H. Xiao, S. Zhao, Q. Lin and Z. Zang, *Laser Photonics Rev.*, 2022, **16**, 2100736.

9 Q. Mo, C. Chen, W. Cai, S. Zhao, D. Yan and Z. Zang, *Laser Photonics Rev.*, 2021, **15**, 2100278.

10 D. Yan, S. Zhao, Y. Zhang, H. Wang and Z. Zang, *Opto-Electron. Adv.*, 2022, **5**, 200075-14.

11 J. Y. Kim, J.-W. Lee, H. S. Jung, H. Shin and N.-G. Park, *Chem. Rev.*, 2020, **120**, 7867–7918.

12 M. I. Hossain, M. Shahiduzzaman, J. H. Rafij, A. Tamang, M. Akhtaruzzaman, A. Hamad, J. Uddin, N. Amin, J.-M. Nunzi and T. Taima, *Mater. Horiz.*, 2024, **11**, 4329–4337.

13 J. H. Park, Y. S. Yoon and J. Y. Kim, *Eco Mat.*, 2023, **5**, e12407.

14 X. Yue, L. Cheng, J. Fan and Q. Xiang, *Appl. Catal., B*, 2022, **304**, 120979.

15 T. Chen, G. Tong, E. Xu, H. Li, P. Li, Z. Zhu, J. Tang, Y. Qi and Y. Jiang, *J. Mater. Chem. A*, 2019, **7**, 20597–20603.

16 A. Pivrikas, H. Neugebauer and N. S. Sariciftci, *IEEE J. Sel. Top. Quantum Electron.*, 2010, **16**, 1746–1758.

17 H. Pan, X. Zhao, X. Gong, H. Li, N. H. Ladi, X. L. Zhang, W. Huang, S. Ahmad, L. Ding, Y. Shen, M. Wang and Y. Fu, *Mater. Horiz.*, 2020, **7**, 2276–2291.

18 T. Wang, W. Deng, J. Cao and F. Yan, *Adv. Energy Mater.*, 2023, **13**, 2201436.

19 W. Peng, K. Mao, F. Cai, H. Meng, Z. Zhu, T. Li, S. Yuan, Z. Xu, X. Feng, J. Xu, M. D. McGehee and J. Xu, *Science*, 2023, **379**, 683–690.

20 A.-N. Cho and N.-G. Park, *ChemSusChem*, 2017, **10**, 3687–3704.

21 J. You, Z. Hong, Y. (Michael) Yang, Q. Chen, M. Cai, T.-B. Song, C.-C. Chen, S. Lu, Y. Liu, H. Zhou and Y. Yang, *ACS Nano*, 2014, **8**, 1674–1680.

22 B. Chen, P. N. Rudd, S. Yang, Y. Yuan and J. Huang, *Chem. Soc. Rev.*, 2019, **48**, 3842–3867.

23 K. Mahmood, S. Sarwar and M. T. Mehran, *RSC Adv.*, 2017, **7**, 17044–17062.

24 Q. Jiang, X. Zhang and J. You, *Small*, 2018, **14**, 1801154.

25 D. Yang, X. Zhou, R. Yang, Z. Yang, W. Yu, X. Wang, C. Li, S. (Frank) Liu and R. P. H. Chang, *Energy Environ. Sci.*, 2016, **9**, 3071–3078.

26 C. Jiang, Z. Zhong, B. Liu, Z. He, J. Zou, L. Wang, J. Wang, J. Peng and Y. Cao, *ACS Appl. Mater. Interfaces*, 2016, **8**, 26162–26168.

27 L. Zang, C. Zhao, X. Hu, J. Tao, S. Chen and J. Chu, *Small*, 2024, **20**, 2400807.

28 L. Lin, T. W. Jones, T. C.-J. Yang, N. W. Duffy, J. Li, L. Zhao, B. Chi, X. Wang and G. J. Wilson, *Adv. Funct. Mater.*, 2021, **31**, 2008300.

29 M. F. M. Noh, C. H. Teh, R. Daik, E. L. Lim, C. C. Yap, M. A. Ibrahim, N. A. Ludin, A. R. bin, M. Yusoff, J. Jang and M. A. M. Teridi, *J. Mater. Chem. C*, 2018, **6**, 682–712.

30 A. Krishnaprasanth and M. Seetha, *AIP Adv.*, 2018, **8**, 055017.

31 H. Szymanowski, O. Zabeida, J. E. Klemberg-Sapieha and L. Martinu, *J. Vac. Sci. Technol., A*, 2005, **23**, 241–247.

32 Z. Wang, J. Lou, X. Zheng, W.-H. Zhang and Y. Qin, *ACS Sustainable Chem. Eng.*, 2019, **7**, 7421–7429.

33 C. Zhang, Y. Shi, S. Wang, Q. Dong, Y. Feng, L. Wang, K. Wang, Y. Shao, Y. Liu and S. Wang, *J. Mater. Chem. A*, 2018, **6**, 17882–17888.

34 R. D. Chavan, M. M. Tavakoli, S. Trivedi, D. Prochowicz, A. Kalam, P. Yadav, P. H. Bhoite and C. K. Hong, *ACS Appl. Energy Mater.*, 2021, **4**, 10433–10441.

35 X. He, J. Wu, X. Li, X. Gao, X. Gan and L. Zhao, *J. Alloys Compd.*, 2009, **478**, 453–457.

36 T. J. Bright, J. I. Watjen, Z. M. Zhang, C. Muratore, A. A. Voevodin, D. I. Koukis, D. B. Tanner and D. J. Arenas, *J. Appl. Phys.*, 2013, **114**, 083515.

37 L. E. Gomes, M. F. da Silva, R. V. Gonçalves, G. Machado, G. B. Alcantara, A. R. L. Caires and H. Wender, *J. Phys. Chem. C*, 2018, **122**, 6014–6025.

38 R. Shao, Z. Cao, Y. Xiao, H. Dong, W. He, Y. Gao and J. Liu, *RSC Adv.*, 2014, **4**, 26447–26451.

39 X. Ling, J. Yuan, D. Liu, Y. Wang, Y. Zhang, S. Chen, H. Wu, F. Jin, F. Wu, G. Shi, X. Tang, J. Zheng, S. (Frank) Liu, Z. Liu and W. Ma, *ACS Appl. Mater. Interfaces*, 2017, **9**, 23181–23188.

40 F. Zhao, Y. Guo, X. Wang, J. Tao, Z. Li, D. Zheng, J. Jiang, Z. Hu and J. Chu, *J. Alloys Compd.*, 2020, **842**, 155984.

41 D. Shen, W. Zhang, Y. Li, A. Abate and M. Wei, *ACS Appl. Nano Mater.*, 2018, **1**, 4101–4109.

42 Y. Zhou, L. M. Herz, A. K.-Y. Jen and M. Saliba, *Nat. Energy*, 2022, **7**, 794–807.

43 X. Cheng, Y. Han and B.-B. Cui, *Adv. Opt. Mater.*, 2022, **10**, 2102224.

44 Y. Li, Y. Wang, Z. Xu, B. Peng and X. Li, *ACS Nano*, 2024, **18**, 10688–10725.

45 G. Kresse and J. Furthmüller, *Comput. Mater. Sci.*, 1996, **6**, 15–50.

46 J. P. Perdew, K. Burke and M. Ernzerhof, *Phys. Rev. Lett.*, 1996, **77**, 3865–3868.

47 D. Han, Y. Xin, Q. Yuan, Q. Yang, Y. Wang, Y. Yang, S. Yi, D. Zhou, L. Feng and Y. Wang, *Sol. RRL*, 2019, **3**, 1900091.

48 Y.-T. Huang, R. Cheng, P. Zhai, H. Lee, Y.-H. Chang and S.-P. Feng, *Electrochim. Acta*, 2017, **236**, 131–139.

49 K. Momma and F. Izumi, *J. Appl. Crystallogr.*, 2008, **41**, 653–658.

50 R. A. Rani, A. S. Zoolfakar, A. P. O'Mullane, M. W. Austin and K. Kalantar-Zadeh, *J. Mater. Chem. A*, 2014, **2**, 15683–15703.

51 J. Buha, D. Arčon, M. Niederberger and I. Djerdj, *Phys. Chem. Chem. Phys.*, 2010, **12**, 15537–15543.

52 A. Krishnaprasanth and M. Seetha, *AIP Adv.*, 2018, **8**, 055017.

53 J. Zhang, Q. Xu, Y. Hu, C. Mao, X. Zhou, M. Lu, M. Zhang, Y. Tong, K. Tang and P. Peng, *Carbon*, 2019, **153**, 104–115.

54 A. Savin, R. Nesper, S. Wengert and T. F. Fässler, *Angew. Chem. Int. Ed. Engl.*, 1997, **36**, 1808–1832.

55 W. Zhang, Z. Zeng, T. Cheng, T. Fei, Z. Fu, X. Liu, J. Zhang and J.-Y. Yang, *Photonics*, 2022, **9**, 440.

56 W. Khan, S. B. Betzler, O. Šipr, J. Ciston, P. Blaha, C. Scheu and J. Minar, *J. Phys. Chem. C*, 2016, **120**, 23329–23338.

57 G. H. de M. Gomes, R. R. de Andrade and N. D. S. Mohallem, *Micron*, 2021, **148**, 103112.

58 G. H. M. Gomes and N. D. S. Mohallem, *Mater. Lett.*, 2022, **318**, 132136.

59 H.-C. Huang and T.-E. Hsieh, *J. Appl. Polym. Sci.*, 2010, **117**, 1252–1259.

60 Y.-N. Wu, L. Li and H.-P. Cheng, *Phys. Rev. B*, 2011, **83**, 144105.